

Project APhiD: A Lorenz-gauged \mathbf{A} - Φ Decomposition for parallelized computation of ultra-broadband electromagnetic induction in a fully heterogeneous Earth

Chester J. Weiss*

Department of Geosciences, Virginia Tech, Blacksburg VA 24061

Abstract

An essential element for computational hypothesis testing, data inversion and experiment design for electromagnetic geophysics is a robust forward solver, capable of easily and quickly evaluating the electromagnetic response of arbitrary geologic structure. The usefulness of such a solver hinges on the balance among competing desires like ease of use, speed of forward calculation, scalability to large problems or compute clusters, [parsimonious](#) use of memory access, accuracy and by necessity, the ability to faithfully [accommodate](#) a broad range of geologic scenarios over extremes in length scale and frequency content. This is indeed a tall order. The present study addresses recent progress toward the development of a forward solver with these properties. Based on the Lorenz-gauged Helmholtz decomposition, a new finite volume solution over Cartesian model domains endowed with complex-valued electrical properties is shown to be stable over the frequency range 10^{-2} – 10^{10} Hz and range 10^{-3} – 10^5 m in length scale. Benchmark examples are drawn from magnetotellurics, exploration geophysics, geotechnical mapping and laboratory-scale analysis, showing excellent agreement with reference analytic solutions. Computational efficiency is achieved through use of a matrix-free implementation of the quasi-minimum-residual (QMR) iterative solver, which eliminates explicit storage of finite volume matrix elements in favor of “on the fly” computation as needed by the iterative Krylov sequence. Further efficiency is achieved through sparse coupling matrices between the vector and scalar potentials whose non-zero elements arise only in those parts of the model domain where the conductivity gradient is non-zero. Multi-thread parallelization in the QMR solver through OpenMP pragmas is used to reduce the computational cost of its most expensive step: the single matrix-vector product at

each iteration. High-level MPI communicators farm independent processes to available compute nodes for simultaneous computation of multi-frequency or multi-transmitter responses.

Keywords: anisotropy, magnetotellurics, CSEM, borehole, geotechnical, radar

1. Introduction

Because of their sensitivity to mineralogy, the presence of fluids and partial melts, and grain-surface chemistry, electromagnetic methods in geophysics have found application in a breadth of geologic problems including mantle and deep crust imaging, to resource exploration, production geotechnical mapping and environmental monitoring. And whereas the question of how best to pair electromagnetic observations with complementary geologic or geophysical data continues to attract attention (Bedrosian, 2007; Gallardo and Meju, 2007; Moorkamp et al., 2011), such efforts are dependent upon the existence of robust and scalable forward solvers that accurately and efficiently capture the physics of electromagnetic induction phenomena in complex geomaterials across a rich spectrum of length scales and frequency content. Progress in addressing the latter question is the focus of the present manuscript.

By necessity, solving electromagnetic induction problems in three dimensions requires the use of numerical methods, and various approaches have been explored for some time now. These include the integral equation method (e.g., Avdeev et al., 2002; Hursan and Zhdanov, 2002), the finite element method (e.g., Bíró and Preis, 1990; Morisue, 1993; Bryant et al., 1998; Sugeng, 1998; Badea et al., 2001; Stalnaker et al., 2006; Mukherjee and Everett, 2011; Schwarzbach et al., 2011; Ribaud et al., 2012; Puzyrev et al., 2013), the finite difference method (e.g., Mackie et al., 1994; Newman and Alumbaugh, 1995; Smith, 1996; LaBrecque, 1999; Tyler et al., 2004; Streich, 2009; Weiss, 2010), and the finite volume method (e.g., Haber and Ascher, 2001; Weiss and Constable, 2006).

Motivated largely by their rich mathematical foundations and the ability of the underlying discretization to conform, at least in a piecewise linear sense, to irregular boundaries

*Corresponding Author: tel (+1) 540-231-3651

Email address: cjweiss@vt.edu (Chester J. Weiss)

Preprint submitted to *Computers & Geosciences*

May 10, 2013

24 between material properties (for example, the contrast of roughly 10 orders of magni-
 25 tude in electrical conductivity *between* air and rock along a topographic profile) the finite
 26 element methods have received comparatively more attention than the others. Early ef-
 27 forts in finite element analysis recognized that the inherent discontinuity of the normal
 28 field components at such conductivity boundaries motivated the use of gauged elec-
 29 tromagnetic potentials which are continuous, although their derivatives (the observable
 30 electromagnetic fields) needn't be. Lorenz-gauged *formulations* with decoupled magnetic
 31 vector and electric scalar potentials are generally incompatible with a nodal based fi-
 32 nite element basis due to continuity requirements at material interfaces B    and Preis
 33 (1990). In contrast, the Coulomb gauged finite elements either in nodal (Badea et al.,
 34 2001; Stalnaker et al., 2006) or edge element basis (Schwarzbach et al., 2011; Mukher-
 35 jee and Everett, 2011; Ribaud   et al., 2012) suffer no such deficiencies. Scripted finite
 36 element solvers such as FlexPDE (<http://www.pdesolutions.com>) and libraries such as
 37 FEMSTER (Castillo et al., 2005) have have been applied for electromagnetic induction
 38 problems over the global (Ribaud   et al., 2012) and basin scales (Schwarzbach et al.,
 39 2011), respectively. Recent advances in domain decomposition of Coulomb-gauged edge
 40 elements for massively parallel computation are found in Puzyrev et al. (2013). A major
 41 impediment to the widespread adoption of finite element methods is the considerable dif-
 42 ficulty in meshing complex geometries, although both open source (TETGEN) (Si, 2007)
 43 and commercial (ANSYS ICEM CFD, <http://www.ansys.com>) are becoming increasingly
 44 accessible.

45 It's worth noting that the choice of gauge is strictly a matter of convenience, based on
 46 the problem at hand. Once such convenience, noted above, is decoupling the potentials
 47 for homogeneous media, which results in a familiar wave equation for both the vector and
 48 scalar potentials. Alternatively, the coupled "action at a distance" Coulomb gauge or
 49 superluminal v-gauge (Brown and Crothers, 1989), also yield equivalent results for the
 50 observable fields (Jackson, 2002) in spite of the non-physical nature of their generative
 51 potentials. Misguided preference for one gauge over another based on causality of the
 52 potentials has apparently been a source of contention within subsets of the induction
 53 modeling community for many years (Bossavit, 1998, p. 274).

54 Finite difference solutions to the Maxwell equations over a staggered grid (Yee, 1966)

Cartesian [discretizations](#) are comparatively simpler and admit the possibility of solving for the fields themselves, rather than the potentials (Mackie et al., 1994; Newman and Alumbaugh, 1995; Weiss and Constable, 2006; Streich, 2009). This avoids the loss of accuracy incurred when numerically [differentiating](#) the potentials, but comes at the cost of solving linear system with a considerable null-space arising from a curl-curl operator in the governing system of partial differential equation. Deflation of the null space is achieved through preconditioning (e.g. Weiss and Newman, 2003) or the use of a static divergence correction (Smith, 1996). [For example, implementation of the simple static divergence correction requires an additional degree of freedom \(the scalar potential\) at grid nodes, thus increasing the number of dependent variable from 3 \(the Cartesian components of the field\) to 4 \(the field plus the potential\). Additional storage requirements from the auxiliary linear solver and its preconditioner can lead to substantial resource overburden. In the more general case of the low-induction number preconditioner \(Weiss and Newman, 2003\) the resource allocation problem is exasperated by the additional requirement of storage for the auxiliary vector potential, bringing the total number of dependent variables from 3 to 7. Although expensive to compute, such corrective procedures often result in solutions to previously \[intractable\]\(#\) problems.](#)

Finite volume solutions are similarly less numerous and have been [considered](#) over Cartesian model domains in either a node-wise (Tyler et al., 2004) or Yee (LaBrecque, 1999; Haber et al., 2000) discretization. In contrast to the finite element case, there exists some degree of flexibility with choice of gauge provided that the underlying discretization is supportive. Face-centered vector potentials with corner-based scalar potentials in the Coulomb gauge is one option (Haber et al., 2000). Another, previously unexplored, is the edge-centered vector potential in the Lorenz gauge. With its companion scalar potential discretized on cell corners, this particular combination of gauge, discretization and formulation of the coupling terms between potentials allows for evaluation of [arbitrary](#) heterogeneous electrical structure and is scalable from low-frequency induction to high-frequency radar. Although recent progress in the application (Schwarzbach et al., 2011; Streich, 2009) of direct linear solvers (Schenk and Gärtner, 2004, 2006; Amestoy et al., 2006) for geo-electromagnetic induction problems has proved promising, the preference here is the work with the [minimal](#) computational footprint offered by sparse [iterative](#)

86 Krylov solvers (Freund and Nachtigal, 1994; Weiss and Constable, 2006), accelerated by
 87 simple Jacobi scaling.

88 This manuscript provides an overview of Lorenz-gauged, coupled magnetic vector \mathbf{A}
 89 and electric scalar Φ decomposition (APhiD) solved for by the finite volume method.
 90 A brief overview of the governing equations for both isotropic and fully generalized
 91 [anisotropic](#) media is given in the Theory section, followed by specific details of the finite
 92 volume stencils, iterative linear solver, and hybrid OpenMP/MPI parallel implementa-
 93 tion in the Methods section. A complementary “scattered field” is found in the Appendix.
 94 Benchmark calculations are drawn from 12 decades in frequency (10^{-2} – 10^{10} Hz) and 8
 95 decades in length scale (mm’s to 10’s of km), spanning applications in magnetotellurics,
 96 marine controlled source [electromagnetics](#), near-surface geotechnical, borehole logging
 97 and laboratory-scale analysis. The magnetotelluric benchmarks are a test of the ac-
 98 curacy of the decoupled vector potentials alone, with no contribution due to the scalar
 99 potential. The remaining examples are thus a test of the complete coupled system subject
 100 to both inductive and grounded source antenna. Effects of model size and heterogene-
 101 ity on linear solver performance appear within the Benchmark section. Comments and
 102 conclusions finalize the paper, with notes on possible approaches for “[focused](#)” precondi-
 103 tioning of the linear solver to accelerate solution convergence in regions of interest within
 104 the model domain.

105 2. Theory

106 Because the magnetic induction field \mathbf{B} is divergence-free, it can be written as the
 107 curl of a magnetic vector potential: $\mathbf{B} = \nabla \times \mathbf{A}$. Assuming an $\exp(i\omega t)$ time dependence,
 108 the electric field \mathbf{E} is given according to Ampère’s Law by both the magnetic vector
 109 potential and the divergence of the electric scalar potential Φ as

$$\mathbf{E} = -i\omega (\mathbf{A} - \nabla\Phi). \quad (1)$$

110 Choosing magnetic permeability as a constant, $\mu_0 = 4\pi \times 10^{-7}$ H/m the usual curl-curl
 111 equation is as follows

$$\nabla \times \nabla \times \mathbf{A} + i\omega\mu_0\hat{\sigma} (\mathbf{A} - \nabla\Phi) = \mu_0\mathbf{J}_s, \quad (2)$$

for an arbitrary 3D electrical conductivity $\hat{\sigma}$ and electric source current density \mathbf{J}_s . Accommodation of the variable magnetic permeability for special geophysical circumstances such as UXO characterization modifies the $\nabla \times \nabla \times$ operator to $\nabla \times \frac{1}{\mu} \nabla \times$. Details of a discrete representation of the latter can be found in (Haber et al., 2000). The electrical conductivity $\hat{\sigma}$ is taken as complex-valued $\hat{\sigma} = \sigma + i\omega\varepsilon$ to accommodate the full physics of field propagation. Through vector identity $\nabla \times \nabla \times \mathbf{A} = -\nabla^2 \mathbf{A} + \nabla(\nabla \cdot \mathbf{A})$, this expression is recast as

$$-\nabla^2 \mathbf{A} + \nabla(\nabla \cdot \mathbf{A}) + i\omega\mu_0\hat{\sigma}(\mathbf{A} - \nabla\Phi) = \mu_0\mathbf{J}_s, \quad (3)$$

where enforcement of the Lorenz gauge $\nabla \cdot \mathbf{A} = i\omega\mu_0\hat{\sigma}\Phi = k^2\Phi$ modifies Eq (3) to read

$$-\nabla^2 \mathbf{A} + k^2 \mathbf{A} + \nabla(k^2\Phi) - k^2\nabla\Phi = \mu_0\mathbf{J}_s. \quad (4)$$

At this point, Eq (4) is a set of three scalar equations and 4 unknowns, and thus, one more equation is required to complete the system of equations. The curl-curl in Eq (2) implicitly enforces $\nabla \cdot \mathbf{J} = 0$, yet such enforcement is lost in the modified form of Eq (4). To regain this requisite property of the total current density, note that

$$\nabla \cdot [k^2(\mathbf{A} - \nabla\Phi)] = \mu_0\nabla \cdot \mathbf{J}_s. \quad (5)$$

Expanding the first term on the left side of Eq (5) and applying the Lorenz condition results in the scalar equation

$$-\nabla \cdot (k^2\nabla\Phi) + k^4\Phi + \nabla \cdot (k^2\mathbf{A}) - k^2\nabla \cdot \mathbf{A} = \mu_0\nabla \cdot \mathbf{J}_s. \quad (6)$$

In operator/matrix form, the complete system of Lorenz-gauged potentials is written as

$$\begin{pmatrix} -\nabla^2 + k^2 & \nabla k^2 - k^2\nabla \\ \nabla \cdot k^2 - k^2\nabla \cdot & -\nabla \cdot k^2\nabla + k^4 \end{pmatrix} \begin{pmatrix} \mathbf{A} \\ \Phi \end{pmatrix} = \begin{pmatrix} \mu_0\mathbf{J}_s \\ \mu_0\nabla \cdot \mathbf{J}_s \end{pmatrix}. \quad (7)$$

Note that the Helmholtz operator in the upper left block of the system matrix works on the vector \mathbf{A} , resulting in three equations; so, too, does the coupling term in the upper right as it computes gradients of Φ and $k^2\Phi$. Therefore the system in Eq (7) is indeed the equivalent 4 equations and 4 unknowns (three components of \mathbf{A} plus Φ) shown earlier in

131 Eqs (4) and (6). Considering the Cartesian components of \mathbf{A} and for brevity, denoting
 132 the Helmholtz operator in the upper left block as $D_1 = -\nabla^2 + k^2$, the coupling terms
 133 in the upper right and lower left blocks as $C_\eta = \partial_\eta k^2 - k^2 \partial_\eta$ over $\eta = x, y, z$ and the
 134 remaining lower right block as $D_2 = -\nabla \cdot k^2 \nabla + k^4$, the system Eq (7) is expanded to
 135 illustrate its sparsity and symmetry in operator form:

$$\begin{pmatrix} D_1 & \cdot & \cdot & C_x \\ \cdot & D_1 & \cdot & C_y \\ \cdot & \cdot & D_1 & C_z \\ C_x & C_y & C_z & D_2 \end{pmatrix} \begin{pmatrix} A_x \\ A_y \\ A_z \\ \Phi \end{pmatrix} = \begin{pmatrix} \mu_0 \hat{x} \cdot \mathbf{J}_s \\ \mu_0 \hat{y} \cdot \mathbf{J}_s \\ \mu_0 \hat{z} \cdot \mathbf{J}_s \\ \mu_0 \nabla \cdot \mathbf{J}_s \end{pmatrix}. \quad (8)$$

136 At this point there are various numerical options for solving the system of equations in
 137 Eq (8) over arbitrary 3D conductivity distribution. In getting to this point, it's been
 138 assumed that the potentials \mathbf{A} and Φ possesses sufficient regularity to allow at least
 139 piecewise manipulation by the operators in Eq (8). For a finite element analysis, a bit
 140 more specificity is required as the requisite function space where \mathbf{A} and Φ reside must be
 141 clearly defined, as must be its finite subset for their discrete representation by the Ritz-
 142 Galerkin method. Here, the finite volume method is chosen instead, both out of simplicity
 143 and to build upon previous work in direct \mathbf{E} field methods (Weiss and Newman, 2002;
 144 Weiss and Constable, 2006).

145 Although the 3D distribution of electrical conductivity in the total field formulation
 146 Eq (7) and (8) admits evaluation of almost arbitrary geologic structure, missing from
 147 the admissible set of models are those geologies which manifest bulk electrical anisotropy
 148 arising from either preferred alignment of intrinsically anisotropic minerals such as mantle
 149 olivine (Constable et al., 1992; Zhang and Karato, 1995) or the coherent organization of
 150 fractures (e.g. Riedel et al., 2012) or sedimentary structure (e.g. Cook et al., 2012). For
 151 completeness, the total field formulation for anisotropic materials is developed below,
 152 although its numerical implementation and examples are reserved for future publication.

153 For the anisotropic case, the magnetic induction \mathbf{B} and electric field \mathbf{E} are decom-
 154 posed via Helmholtz's theorem as before for the isotropic case Eq (1) and preceding text.

Let $\hat{\sigma}$ denote the symmetric, rank-2, complex-valued electrical conductivity tensor consisting of $\text{diag}(\sigma_{x'x'}, \sigma_{y'y'}, \sigma_{z'z'})$ in the (x', y', z') principal axes reference frame, rotated into the (x, y, z) model domain by the orthogonal rotation matrix \mathbf{R} . In general, this representation results in six degrees of freedom: one for each conductivity value in the primed coordinate system, plus three Euler angles (or directional cosines) for construction of \mathbf{R} . In transverse isotropic media, where two principal conductivity values are equivalent, as is the case for anisotropy arising from laminated or “platy” materials, the number of degrees of freedom reduces to only four, even when $\hat{\sigma}$ is fully populated with non-zero elements. Note that the principal conductivities and the corresponding rotation matrix are each functions of position. Note, too, that the rotation matrix applies to both the real (induction) part of the conductivity and the imaginary (wavelike) part. In principle, one could conceive of one principal axes reference frame for the low-frequency induction response and different one for the high-frequency wave response, resulting in the maximum 12 degrees of freedom for the 3×3 complex valued tensor $\hat{\sigma}$.

As a result of this (even) more general representation of the electrical conductivity, the curl-curl Eq (2) is recast as

$$\nabla \times \nabla \times \mathbf{A} + i\omega\mu_0 \hat{\sigma} \cdot (\mathbf{A} - \nabla\Phi) = \mu_0 \mathbf{J}_s. \quad (9)$$

Again, sticking with the Lorenz gauge, let $\nabla \cdot \mathbf{A} = i\omega\mu_0 \hat{\sigma}^*$ where $\hat{\sigma}^*$ is a convenient, complex scalar value of complex conductivity whose value we are free to fix at a later time. Substituting the gauge condition into Eq (9) yields an expression similar to Eq (4) for the scalar case, plus an additional term:

$$-\nabla^2 \mathbf{A} + k^2 \mathbf{A} + \nabla(k^2 \Phi) - k^2 \nabla\Phi + \mathbf{k} \cdot (\mathbf{A} - \nabla\Phi) = \mu_0 \mathbf{J}_s, \quad (10)$$

where $k^2 = i\omega\mu_0 \hat{\sigma}^*$, as before, and the symmetric rank-two tensor $\mathbf{k} = i\omega\mu_0 (\hat{\sigma} - \hat{\sigma}^* \mathbf{I})$. Choosing $\hat{\sigma}^* = \frac{1}{3} \text{Tr}(\hat{\sigma})$ results in zero-values for the last 2 terms on the left side of Eq (10) in regions where the conductivity is isotropic, thus reducing Eq (10) to Eq (4) in these regions. An extra term, analogous to the one just discussed in Eq (10), appears in the generalization of current conservation Eq (6) to anisotropic media,

$$-\nabla \cdot (k^2 \nabla \Phi) + k^4 \Phi + \nabla \cdot (k^2 \mathbf{A}) - k^2 \nabla \cdot \mathbf{A} + \nabla \cdot [\mathbf{k} \cdot (\mathbf{A} - \nabla \Phi)] = \mu_0 \nabla \cdot \mathbf{J}_s, \quad (11)$$

which also vanishes in regions of the model where anisotropy is absent.

3. Method

As a starting point, note that third and fourth terms on the left side of Eq (4) could easily be simplified as $\Phi \nabla k^2$. However, also observe that in doing so, a numerical discretization of Eq (4) either requires co-location of Φ and \mathbf{A} on the underlying grid, or requires some averaging scheme for Φ to collocate its estimate on the grid with \mathbf{A} . Because our electric field is a sum of \mathbf{A} and the gradient of Φ , co-location is not optimal – one would prefer co-location of \mathbf{A} and $\nabla \Phi$ instead. The staggered (Yee, 1966) grid offers such an option where Φ is located on the nodes of a Cartesian grid, and components of \mathbf{A} parallel to the grid edges are located at the midpoints of those corresponding edges. In such a discretization, a given component of $\nabla \Phi$ is most accurately estimated (via central differences) at the edge midpoint, co-located with the corresponding \mathbf{A} component. Thus, components of \mathbf{E} along mesh edges are well defined. If we choose mesh cells to represent regions of uniform electrical conductivity, one also finds that the primary merit of the Yee grid is preserved: the only components of electric field in the discretization are those that lie parallel to conductivity boundaries. Thus, continuity of tangential electric field across conductivity jumps is inherently preserved in the discretization.

Implementation of the Yee grid in a finite volume approximation to Eq (8) is as follows. Starting with a tensor-product Cartesian grid consisting of nodes x_1, x_2, \dots, x_{N_x} in the \hat{x} direction, y_1, y_2, \dots, y_{N_y} in \hat{y} and z_1, z_2, \dots, z_{N_z} in \hat{z} , let the vector $\mathbf{u}^T = (\mathbf{A}_{\mathbf{x}}^T, \mathbf{A}_{\mathbf{y}}^T, \mathbf{A}_{\mathbf{z}}^T, \Phi^T)$ represent discrete values of vector and scalar potentials on the mesh edges and nodes, as described above. The hexahedral cells defined by this grid are each endowed with an arbitrary value of complex conductivity, with the real component representing the diffusive, Ohmic conductivity and the imaginary component representing the product of absolute electric permittivity and angular frequency. Observe, however, that the staggered Yee grid leads to a finite volume formulation built around the dual (Voronoi) grids for the x , y and z edges plus a dual grid centered on the nodes (Figure

1). Because of the rectilinear geometry of the Cartesian mesh, each of these dual grids, in turn, is a rectilinear grid, differing from one another only in the edges and nodes of the primal grid which lie at the center of their respective Voronoi cells. Integrating the first block row of equations in (8) over dual grid cells for x edges (Figure 1) leads to the well-known 7-point stencil for the Helmholtz term D_1 (Figure 2) plus simple differences of Φ for the coupling term C_x (Figure 3). For example, the product of C_x with Φ at for edge centered at $i + \frac{1}{2}, j, k$ is

$$\left(\frac{k_{i+1,j,k}^2 - k_{i+\frac{1}{2},j,k}^2}{x_{i+1} - x_i} \right) \Phi_{i+1,j,k} - \left(\frac{k_{i,j,k}^2 - k_{i+\frac{1}{2},j,k}^2}{x_{i+1} - x_i} \right) \Phi_{i,j,k}. \quad (12)$$

Hence, operator D_1 is approximated in a finite volume sense by a $(N_x - 1)N_y N_z \times (N_x - 1)N_y N_z$ sparse matrix \mathbf{D}_1 with 7 non-zero elements per row, and C_x by a $(N_x - 1)N_y N_z \times N_x N_y N_z$ sparse matrix \mathbf{C}_x with only 2 non-zero elements per row. Approximating the remaining operators in Eq (8) in a similar way results in $M \times M$ global coefficient matrix \mathbf{K} given by

$$\mathbf{K} = \begin{pmatrix} \mathbf{D}_1 & \cdot & \cdot & \mathbf{C}_x \\ \cdot & \mathbf{D}_1 & \cdot & \mathbf{C}_y \\ \cdot & \cdot & \mathbf{D}_1 & \mathbf{C}_z \\ \mathbf{C}_x^T & \mathbf{C}_y^T & \mathbf{C}_z^T & \mathbf{D}_2 \end{pmatrix}, \quad (13)$$

where $M = (N_x - 1)N_y N_z + N_x(N_y - 1)N_z + N_x N_y(N_z - 1) + N_x N_y N_z$. The right hand side \mathbf{s} of the finite volume linear system resulting from Eq (8) is simply constructed by integration of the source current density \mathbf{J}_s and its divergence over cells of their corresponding Voronoi grids.

The finite volume system of linear equations

$$\mathbf{K}\mathbf{u} = \mathbf{s} \quad (14)$$

with complex-symmetric coefficient matrix \mathbf{K} is solved iterative by a two-term coupled recurrences implementation of the quasi-minimal-residual (QMR) method (Freund and

226 Nachtigal, 1994; Weiss and Constable, 2006), accelerated by simple Jacobi scaling and
 227 memory-optimized with a matrix-free implementation (Weiss, 2001). The initial solution
 228 estimate \mathbf{u}_0 is taken as the zero vector, and QMR updates $\mathbf{u}_1, \mathbf{u}_2, \dots$ are computed until
 229 the L_2 residual $\|\mathbf{K}\mathbf{u}_i - \mathbf{s}\|$ at iteration i is either sufficiently reduced by some factor τ
 230 over the initial residual or if a pre-determined number of maximum iterations is met.
 231 Typical values of τ for acceptable solution accuracy are in the range $10^{-8} - 10^{-12}$, with
 232 convergence occurring in as few as a couple hundreds of iterations and upwards to the
 233 low thousands for particularly ill-conditioned systems described later.

234 Observe that values of k^2 in Eq (12) with half-integer indices are those along edges and
 235 thus require the 4-cell averaging scheme for adjacent cells, whereas values with whole-
 236 integer indices are node based with values computed by neighboring 8-cell averaging. In
 237 regions where these two averaging schemes give equal values, elements of the discrete
 238 coupling matrices are identically zero, as expected.

239 A subtle point to observe in the construction of the right side for the total field for-
 240 mulation is that integration of filamentary source currents (and their divergence) is most
 241 accurate if those filaments are coincident with the the edges of the primal finite volume
 242 grid (Figure 4). Treatment of the right hand side of Eq (8) in a strict finite difference
 243 formulation is difficult if the source currents are filamentary, infinitesimally thin, and not
 244 coincident with mesh edges. One approach to skirting the problem is to work with the
 245 scattered field formulation developed in the Appendix, choosing the reference conduc-
 246 tivity $\hat{\sigma}_0$ sufficiently simple (for example, a uniform whole space) such that computation
 247 of the primary potentials is cheap. An alternative is to consider some averaging scheme
 248 where a small assemblage grid-locked finite current elements is a sufficient approxima-
 249 tion to the true source current. For the computational examples given here, a total-field
 250 formulation is used and the source current is simply taken as coincident with the grid
 251 with a minimum length equal to the edge upon which it's located. For example, the
 252 current element $\mathbf{J}_s = \hat{x}I\delta(y - y_j)\delta(z - z_k)(H(x - x_i) - H(x - x_{i+1}))$, with δ represent-
 253 ing Dirac's delta function and H the Heaviside function, is easily compatible with the
 254 integration procedure described earlier, yielding non-zero values in both the $\mu_0\mathbf{J}_s$ and
 255 $\mu\nabla \cdot \mathbf{J}_s$ components for their discrete form in the right hand side of Eq (14).

256 Implementation of the preceding steps is done in a hybrid parallel decomposition

257 over functional and spatial (grid) domains (Figure 5). Observing that the coefficient
 258 matrix of the finite volume system of linear equations is structured such that the first
 259 $(N_x - 1)N_yN_z$ rows of Eq (14) correspond to discretization of the x component of Eq (4),
 260 with the next $N_x(N_y - 1)N_z$ corresponding to the y component and so on, contraction of
 261 this matrix with Krylov vectors during the iterative QMR sequence can be done easily
 262 in parallel with no message passing requirements. These computations are parallelized
 263 over 4 threads through OpenMP pragmas, thus reducing the cost of this relatively ex-
 264 pensive step in a given QMR iterate up to factor of four, depending on problem size and
 265 hardware architecture. For completeness, the remaining inner products, norms, etc, in
 266 the remaining steps of a given QMR iterate, but their impact on reducing the run time is
 267 far less dramatic. Lastly, a high-order functional decomposition is imposed at the onset
 268 through MPI pragmas to allow for an array of frequencies to be computed, independently,
 269 over concurrent parallel processes. It also allows for the special case of magnetotelluric
 270 sounding (e.g. Weiss, 2012) where the response of two independent polarizations of \mathbf{J} are
 271 required for impedance tensor calculation.

272 4. Benchmarking

273 In keeping with the distinction in nomenclature pointed out by Oreskes et al. (1994)
 274 for seemingly interchangeable terms as “validation”, “verification”, the following section
 275 focuses on comparisons between the fields deriving from solution to Eq (8) and inde-
 276 pendent solutions derived from independent methods, specifically, “benchmarking.” The
 277 models herein are motivated by ones relevant to the Earth sciences and, in particular,
 278 exploration geophysics, but should not be interpreted as exhausting the potential applica-
 279 tion areas for the APhiD algorithm. Indeed, their purpose is simply to provide a context
 280 for testing the algorithm and to provide guidance for the end user in the important area
 281 of mesh design. **In each example a homogeneous Neumann boundary condition is applied**
 282 **out of convenience, the effects of which are generally constrained to the outermost layers**
 283 **of cells of the mesh.**

284 4.1. Reduction to Scalar Helmholtz: The 1D MT Example, $f < 1\text{Hz}$

285 It is straightforward to demonstrate that for a horizontal “sheet” current at some
 286 distance h above the surface of a horizontally layered Earth (a.k.a. 1D magnetotelluric

problem) the magnetic vector and electric potentials decouple and simplify, leaving a single, scalar Helmholtz equation in terms of the single component of magnetic vector potential parallel to the source current. Scaling this potential by $i\omega$ yields the electric field in accordance with Eq (1). A similar simplification is apparent in Eq (8), if for example, one takes the z direction as downward with $z = 0$ representing Earth’s surface, defines a unit source current density $\mathbf{J}_s = \delta(z + h)$ and sets the conductivity model $\hat{\sigma}(x, y, z > 0)$ as depending on z only. Hence, the simplest benchmark is to verify that the potentials in Eq (8) decouple as expected, and that the numerical results are consistent with corresponding analytic solutions.

Considered here is a simple N-layer MT model, fashioned loosely after representative values for continental conductivities and thickness, including a thin, conductive mid-crustal conductor (e.g. Hermance and Neumann, 1991; Jones et al., 2003). The model is defined as follows: 19 km of resistive 0.001 S/m upper crust overlying a thin 1 km layer of elevated 0.1 S/m conductivity resting atop a semi-infinite 0.01 S/m lower crust. Air conductivity is taken as 10^{-8} S/m. Analytic solutions for such a model are readily available (e.g. Wait, 1962; Chave and Weidelt, 2012) and are easily shown to take the form $e^{\pm kz}$ within a given layer.

Sensitivity of surface-based MT measurements to the 0.1 S/m mid-crustal conductor requires operating frequencies less than a few Hertz. As such, direct comparisons between analytic and numeric solutions at 0.01, 0.1 and 1.0 Hz (Figures 6-8) illustrate the rapid attenuation with depth of the magnetic field within the thin conducting layer. At the highest frequencies, the layer acts as “geo-Faraday” cage, attenuating nearly all electric and magnetic field and propagating little into the lower crustal region below. Lower frequencies demonstrate, as expected, a diminished effect, with strongly propagating fields deep into the lower crust.

Finite volume models are built on a Cartesian mesh of $50 \times 50 \times 121$ cells in x , y and z . Horizontal mesh nodes are evenly distributed over ± 50 km for all models. Vertical mesh nodes are also evenly distributed, albeit in a piecewise fashion: 51 cell layers, each 1.961 km thick in the air region; 19 layers, each 1 km thick in the upper crust; and, 20 layers, each 0.5 km thick in the mid crustal conductor. For the 0.01 Hz low frequency model the remaining 30 layers within the lower crust are evenly distributed over 120 km for a

layer thickens of 4km whereas for the other two high frequency models, layer thickness is reduced to 1 km, resulting in a 50 km terminal depth of the model domain. Discrepancy between the analytic and numerical solutions for the mid-frequency model (0.1 Hz) at depths below 35 km are an artifact of the mesh boundary generating scattered fields that propagate back toward the mesh interior. Such an effect is not seen in the rapidly attenuating, high-frequency 1.0 Hz results and the low-frequency results where the mesh terminates at 140 km depth. Runtimes for a $\tau = 10^{-10}$ residual reduction are on the order of 200 s over a single CPU core.

4.2. Mixed 3D Inductive/Galvanic Coupling: Electric Dipole Antennae at the Basin Scale, $f \sim 1\text{Hz}$

Recent interest in electromagnetic methods for hydrocarbon exploration and reservoir monitoring in marine environments (e.g. Constable and Weiss, 2006; Weiss and Constable, 2006; Constable and Srnka, 2007) motivates the question of applicability of the $\mathbf{A} - \Phi$ method to such problems. In particular, the source antenna for the marine controlled-source electromagnetic (CSEM) problem consists of a finite dipole with inductive coupling to the earth along its length and galvanic coupling at its ends due to its un-insulated tips. Modeling this antenna, therefore, requires both the \mathbf{J}_s and $\nabla \cdot \mathbf{J}_s$ terms, respectively, in the source current specification. As such, modeling the CSEM problem is a test, even in layered-earth geometries, of the full coupling between the complete magnetic field vector \mathbf{A} and electric scalar Φ potentials. Furthermore, analysis of electric fields according to Eq (1) provides an assessment of the combined solution accuracy for both the magnetic vector \mathbf{A} and electric scalar Φ potentials.

As such, two exploration scenarios were considered: one for “deep” water where the effects of a finite water column on seabed electric fields are indistinguishable from those of an infinitely deep water column; and the other, a “shallow” water problem where the effect of ocean-atmosphere coupling dominate the seabed electromagnetic response, especially at long transmitter-receiver offsets. In each, the 1 Hz transmitter is modeled as a finite electric dipole extending in length over the edge of a single grid cell, and suspended in the 3.2 S/m seawater a distance 100 m above a 1.0 S/m “sediment” halfspace (Figure 9, inset). Numerical results for the deep water model (Figure 9, top panels) are

348 based on an un-optimized mesh of $101 \times 101 \times 101$ nodes, uniformed distributed over
 349 $|x|, |y|, |z| < 5$ km. Agreement between analytic (Wait, 1962; Baños, 1966) and numeric
 350 solutions is excellent for the inline electric fields computed along the sea bed. For the
 351 shallow-water example, a slightly modified mesh was used in order to accommodate the
 352 weakly-attenuating field propagation through the air region of the model. As such, the
 353 101 horizontal grid nodes in x and y were geometrically distributed over a slightly larger
 354 area $|x|, |y| < 20$ km, with a 3% increase in node separation as a function of distance
 355 from the origin. In the vertical direction z the air layer is 20 km thick, within which
 356 are 30 node intervals geometrically distributed at a 5% increase in node separation from
 357 the air-sea interface. Within the 500 m deep water column are 20 node intervals, evenly
 358 spaced. Below that are 30 intervals over 9500 m, again geometrically distributed with
 359 a 5% increase in spacing with depth. Again, agreement between the analytic solution
 360 and numeric solution is excellent for the inline electric fields along the seabed (Figure 9,
 361 bottom panels), confirming that the electric potential, too, is computed accurately.

362 For the deep water models, QMR convergence rate of the log-residual as a function
 363 of transmitter frequency is roughly linear, with more rapid convergence observed for the
 364 higher frequencies when the coefficient matrix in Eq (14) becomes increasingly diagonally
 365 dominant (Figure 10, top panels). The same behavior holds for meshes four times the
 366 size (Figure 10, bottom panels). Keeping the mesh geometry constant, including an
 367 air layer leads to slight increase in iteration count to achieve the same level of residual
 368 reduction τ , a slowdown that occurs after the ~ 100 iterations for these particular models.
 369 Note, however, that convergence with the air layer required no special intervention via
 370 static divergence correction (Smith, 1996), its more general “low induction number”
 371 preconditioner (Newman and Alumbaugh, 2002; Weiss and Newman, 2003) or alternative
 372 and costly preconditioning schemes such as incomplete LU or Cholesky, as is often done
 373 for \mathbf{E} or \mathbf{H} field formulations of the governing Maxwell equations.

374 *4.3. Pure Inductive Coupling: Magnetic Dipole Antennae at Geotechnical Scale, $f \sim$* 375 *1kHz*

376 Of particular interest to geotechnical community are accurate and rapid solutions
 377 for commercial instrumentation. Considered next, in this section, is a simulation the

378 Geonics EM-34 ground conductivity meter in “vertical dipole” mode and intermediate
 379 20 m source-receiver spacing. For these particular examples the mesh is built on $100 \times$
 380 100×101 nodes over $|x|, |y| < 150$ m and $-400 \text{ m} < z < 150$ m, with $z = 0$ representing
 381 the air–earth interface. Of the 100 cell layers in z defined by this mesh, 50 are allocated
 382 for each of the air and earth regions, resulting in roughly equidimensional cells with edge
 383 length ~ 3 m in the $z > 0$ earth region, and elongated to 8 m tall in the $z < 0$ air region.
 384 Permittivity is that of free space throughout the model domain. Air conductivity is fixed
 385 at 10^{-8} S/m, with earth conductivity set to 1.0 S/m for the conductive model test and
 386 the 0.1 S/m for the “resistive” model test. Considering both conductivity models on a
 387 single grid is designed to test the robustness of a particular discretization to variations in
 388 electrical conductivity – a necessary property for its use in geophysical inversion
 389 where it is common to for inversion algorithms to evaluate multiple model realizations
 390 on a single fixed grid.

391 The EM-34 circular transmitter loop of diameter 0.6 m (or 1.0 m for the XL) model
 392 is approximated by a square current loop of dimension 3.03×3.03 m lying directly
 393 on the air–earth interface and excited at 1 kHz. Comparison of the vertical induction
 394 field B_z to analytic solution for an infinitesimal vertical magnetic dipole source (Ward
 395 and Hohmann, 1987) yields excellent results (Figure 11) for both conductivity models,
 396 both in the imaginary component used by the EM-34 instrument for ground conductivity
 397 estimation, and the unused real component. Note the strong agreement between solutions
 398 at the 20 m offset used in EM-34 profiling at the 1.6 kHz operating frequency. Evidence
 399 of the near-field signature of the square transmitter is suggested by the slight discrepancy
 400 between solutions in the shortest offsets. Also evident at the longest offsets are the effects
 401 the mesh boundary “leaking” into the mesh interior. QMR sequence was terminated after
 402 837 iterations over 590 s at a residual reduction factor of $\tau = 10^{-14}$. Reducing the target
 403 residual to $\tau = 10^{-6}$ led to convergence after 490 iterations over 313 s. Such behavior of
 404 initially slow convergence followed by rapid convergence is typical of models containing
 405 an air layer (Figure 10).

4.4. High-Frequency Borehole Induction Logging, $f = 5$ MHz

The mesh is composed of $60 \times 60 \times 121$ nodes distributed with piecewise constant spacing on ± 2.2 m in x and y , and ± 10 m in z , with the z -direction taken as parallel to the borehole axis. Node spacing in z increases at a rate of 5% per node from the $z = 0$ plane, starting with an initial spacing of 0.028 m and terminating with spacing 0.51 m at the $\pm z = 10$ m mesh boundaries. Node spacing in x and y is piecewise constant, taking the value 0.02 m for $|x|, |y| < 0.41$ m and 0.2 m elsewhere (Figure 12). Throughout the mesh the relative dielectric constant is set to unity, however, the conductivity is variable, representing a bed boundary with a normal incidence borehole filled with conducting drilling fluid (Figure 13, inset). Conductivity of the 0.20 m diameter borehole is 1.25 S/m, with 100:1 contrast bed conductivities, taking values 1 S/m for the upper bed and 0.01 S/m for the lower. The source is represented as a finite square loop in $z = 0$ plane over one cell facet, with unit current density and sides of length 0.02 m resulting in a dipole moment of 4×10^{-4} A-m².

Note that conductivity boundaries models such as this do not naturally conform the rectilinear grid used by APhiD or previously published finite difference solutions (e.g. Mackie et al., 1994; Newman and Alumbaugh, 1995; Avdeev et al., 2002). As a result, the curved boundary of the borehole/formation contact is reasonably well represented by a staircase boundary when considering field values along the borehole axis in spite of well-known problems with representing curved boundaries on rectilinear grids (Holland, 1993). Accurate computation of fields on the borehole perimeter may require a more sophisticated meshing scheme such as triangulated finite differences (Weiss, 2010) or some volume-weighted averaging of cell conductivities for cells intersecting the borehole wall (Newman and Alumbaugh, 2002). Such analyses are beyond the scope of the current study, and for the receiver array considered here, reasonable agreement is observed between numerical and integral equation solutions for the receivers along the simulated borehole array. Note that differences between the solutions at extremely short offsets, less than roughly 0.3 m, are due to the difference between an idealized point dipole field of the integral equation solution and the more realistic finite source used in the numerical solution. And although the antenna and discretized borehole perimeter do not exhibit the strict azimuthal symmetry possessed by the integral equation solution, the

intrinsic conductivity averaging along the borehole perimeter described in Section 3 and the far-field location of receiver array results in no demonstrable solution degradation. The QMR iterative sequence was terminated after 1000 iterations taking 298 s, during which the residual error was reduced by a factor of $\tau \sim 10^{-9}$.

4.5. Dielectric Effects and Lab-Scale Radar Analysis, $f = 10$ GHz

To accommodate the grain-scale structure of rocks at the laboratory or hand-specimen scale, the following simulations are done with a mesh composed of $70 \times 70 \times 71$ nodes even distributed over a 0.1 m cube. Electrical conductivity σ throughout the volume is given a constant value of 0.5 S/m. Relative dielectric constant ε_r in the $z < 0$ region is equal to 1, with that in the $z > 0$ region set to 2 to isolate the effects of dielectric heterogeneity on electromagnetic response. Out of simplicity, and building on previous numerical simulation examples, the source is again a square loop antenna centered at the middle of the mesh along the contact between halfspaces, coincident with a single mesh facet measuring 1.4 mm on a side. Results are normalized by a factor 4.76×10^5 for the equivalent unit-dipole response.

An operating frequency of 10 GHz results in damped, propagating waves within the sample that respond to both conductivity σ and dielectric properties $\varepsilon = \varepsilon_0 \varepsilon_r$, attenuating as a function of distance (skin depth) from the receiver. Considering the complex wavenumber $k^2 = -i\omega\mu_0(\sigma + i\omega\varepsilon_0\varepsilon_r)$ for regions of constant electrical properties, the predicted whole-space wavelengths of 0.021 m and 0.027 m are evident in the $z < 0$ and $z > 0$ regions, respectively, of the solution domain (Figure 14). Furthermore, the $z > 0$ region, with its higher relative dielectric constant and shorter wavelength, illustrates weaker attenuation of the wave amplitude, corresponding to a skin depth of 0.0154 m. In contrast, the long-wavelength $z < 0$ region confirms the expected result of rapid attenuation with skin depth 0.0115 m. For reference, the fields along the $z = 0$ interface (Figure 15) exhibit the expected azimuthal symmetry for the far field solution of the loop source. Comparison with analytic solution along this interface shows excellent agreement (Figure 16), with the expected mesh boundary results degrading the solution in regions farthest from the source. Solution time for a reduction in solution residual by a factor of $\tau = 10^{-12}$ over 397 QMR iterations was 102 s.

467 5. Conclusions

468 The finite volume solution for full-spectrum, Lorenz-gauged potentials (APhiD) has
 469 been developed here for both isotropic and generalized anisotropic geomaterials. Bench-
 470 marking examples over the frequency range 10^{-2} – 10^{10} Hz and spatial length scales 10^{-3} –
 471 10^5 m show consistently excellent agreement with analytic and quasi-analytic reference
 472 solutions for planewave, electric [dipole](#), magnetic dipole and finite loop source anten-
 473 nae for systems [possessing](#) both conductivity and dielectric heterogeneity. These exam-
 474 ples represent a broad range of possible geophysical application areas for the proposed
 475 APhiD method, including: magnetotellurics, marine controlled source electromagnetics,
 476 near-surface geotechnical surveys, borehole induction logging/radar, and laboratory-
 477 scale analysis.

478 The APhiD method differs from previous discrete solution methods in its use of the
 479 Lorenz gauge and a matrix-free implementation of the QMR linear solver. The latter has
 480 been previously applied to direct field [formulations](#) (Weiss, 2001) but not to potential field
 481 formulations. Weiss (2001) demonstrated that “on the fly” calculation of matrix elements
 482 of the finite difference coefficient matrix at each QMR iteration came at a competitive
 483 (and some cases, lower) computational cost when compared to CPU cache hits from
 484 the non-sequential data access required for sparse matrix-vector multiply. The resulting
 485 storage savings for an $N \times N$ linear system is a reduction from $25N$ to $12N$ complex
 486 double precision words. A similar reduction in storage costs is realized in the APhiD
 487 approach, although the savings are model-dependent. The reason lies in the structure of
 488 the coupling matrices $\mathbf{C}_{\mathbf{x}} \dots$ in Eq (13). Observe that these matrices possess non-zero
 489 elements for those edges/nodes where $\nabla \hat{\sigma}$ is also non-zero as revealed by discretization of
 490 $\nabla k^2 \Phi - k^2 \nabla \Phi$ for the upper 3 block-rows and $\nabla \cdot k^2 \mathbf{A} - k^2 \nabla \cdot \mathbf{A}$ for the bottom block-row.
 491 Rows of Eq (13–14) where the complex conductivity gradient is zero therefore contain
 492 only 7 non-zero elements arising from discretization of the Helmholtz operator in \mathbf{D}_1
 493 and \mathbf{D}_2 . Therefore, contraction of the matrix \mathbf{K} with a given Krylov vector in the QMR
 494 iterative sequence requires at least $7N$ but no more than $10N$ complex [multiplications](#).
 495 If a stored-matrix solver is to be considered in some future study, the sparsity of the
 496 coupling matrices derived from Lorenz gauge can reduce the matrix storage cost by as
 497 much as 30%. In contrast, the Coulomb gauge (Haber et al., 2000) formulation yields a

fixed template of non-zero elements within the coupling matrix due to its discretization of the $\nabla \cdot$ operator, therefore resulting in a fixed storage/floating point cost of $10N$ for magnetically homogeneous media.

Further performance differences from the Coulomb gauge formulation are revealed by the effect of frequency ω on linear solver convergence. Haber et al. (2000) and Haber and Ascher (2001) examined this effect on models consisting of buried blocks and random media, and generally found that as frequency increases, so too, does the requisite number of iterations to achieve a given reduction in error residual. This is in sharp contrast to the results presented in the current study in Figure (10), where an increase in frequency for the “deep water” marine CSEM models resulted in a significant reduction in QMR iterations – up to a factor of four for a modest frequency increase from 0.1 Hz to 10 Hz. Inclusion of the air layer neutralized this high-frequency advantage for the models tested. Note that as frequency is increased, the discrete forms of Helmholtz operators D_1 and D_2 in Eq (8) become increasingly diagonally dominant. In contrast, the Poisson operator corresponding to D_2 in the Coulomb gauge simply scales each element of its discrete analogue by the same constant, with no special treatment given to the diagonal elements alone.

While the QMR solver with Jacobi preconditioning is shown here to be a reliable and fast solution method to the finite volume system of linear equations Eq (14), it is observed that iterative refinement of the QMR solution estimate is non-uniform throughout the domain, typically converging fastest near the source and more slowly elsewhere (Fig 17). From the perspective of evaluating how the fields behave throughout the entire modeling domain, this is simply an interesting observation of the method’s efficiency. However, from the perspective of generating model results where the field values at a few select points of the model domain are required for comparison with observed data, as is the case with the geophysical inverse problem, it would be beneficial to explore the possibility of guiding the QMR update sequence to converge most rapidly on the observation points themselves. Hence, a modified or “focused” residual norm (FRN), perhaps something of the form $\|\text{diag}(w_1, w_2, \dots) (\mathbf{K}\mathbf{u}_i - \mathbf{s})\|$, where the weights w are selected to emphasize the relative contribution of the residual in the region of interest, could be introduced into the formulation of QMR algorithm (or related Krylov methods) as the quantity to be

minimized. Clearly such an effort is beyond the scope of this paper, but merits further investigation as a practical way toward minimizing the computational cost of the 3D inverse problem.

6. Acknowledgments

CJW is grateful to Didem Beskardes and Glenn Wilson for helpful comments during the manuscript preparation. The thoughtful consideration of the editor and reviewers is greatly appreciated, without whose suggestions the manuscript demonstrably suffered. Financial support was generously provided through the Hydrologic Sciences Program of the United States National Science Foundation, award number EAR-0943598.

7. Bibliography

- Amestoy, P. R., Guermouche, A., L'Excellent, J.-Y., Pralet, S., 2006. Hybrid scheduling for the parallel solution of linear systems. *Parallel Computing* 32, 136–156.
- Avdeev, D. B., Kuvshinov, A. V., Oleg, Pankratov, Newman, G. A., 2002. Three-dimensional induction logging problems, Part I: An integral equation solution and model comparisons. *Geophysics* 67, 413–426.
- Badea, E. A., Everett, M. E., Shen, L. C., Weiss, C. J., 2001. Effect of background fields on three-dimensional finite element analysis of induction logging. *Radio Science* 36, 721–729, doi:10.1029/2000RS002576.
- Baños, A., 1966. *Dipole Radiation in the Presence of a Conducting Half-Space*. Pergamon Press, Oxford.
- Bedrosian, P., 2007. MT+, integrating magnetotellurics to determine earth structure, physical state, and processes. *Surveys in Geophysics* 28, 121–167, doi:10.1007/s10712-007-9019-6.
- Bíró, O., Preis, K., 1990. Finite element analysis of 3-D eddy currents. *IEEE Transactions on Magnetics* 26, 418–423.
- Bossavit, A., 1998. *Computational Electromagnetism*. Academic Press, San Diego CA.
- Brown, G. J. N., Crothers, D. S. F., 1989. Generalized gauge invariance in electromagnetism. *Journal of Physics – A: Mathematical and General* 22, 2939–2959.
- Bryant, C. F., Emson, C. R. I., Trowbridge, C. W., Fernandez, P., 1998. Lorentz gauge formulations for eddy current problems involving piecewise homogeneous conductors. *IEEE Transactions on Magnetics* 34, 2559–2562.
- Castillo, P., Rieben, R., White, D., 2005. FEMSTER: An object oriented class library of high-order differential forms. *ACM Transactions on Mathematical Software* 31, 425–457, doi:10.1145/1114268.1114269.
- Chave, A., Weidelt, P., 2012. Chapter 2. The theoretical basis for electromagnetic induction. In: Chave, A., Jones, A. (Eds.), *The Magnetotelluric Method: Theory and Practice*. Cambridge University Press, pp. 19–49.

563 Constable, S., Shankland, T., Duba, A., 1992. The electrical conductivity of an isotropic olivine mantle.
564 Journal of Geophysical Research: Solid Earth 97, 3397–3404.

565 Constable, S., Srnka, L., 2007. An introduction to marine controlled-source electromagnetic methods
566 for hydrocarbon exploration. Geophysics, WA3–WA12.

567 Constable, S., Weiss, C. J., 2006. Mapping thin resistors and hydrocarbons with marine EM methods
568 — Insights from 1D modeling. Geophysics 71, G43–G51.

569 Cook, A. E., Anderson, B. I., Rasmus, J., Sun, K., Li, Q., Collett, T., Goldberg, D. S., 2012. Electrical
570 anisotropy of gas hydrate-bearing sand reservoirs in the Gulf of Mexico. Marine and Petroleum Geology
571 35, 72–84.

572 Freund, R., Nachtigal, N., 1994. An implementation of the QMR method based on coupled two-term
573 recurrences. SIAM Journal of Scientific and Statistical Computing 15, 313–337.

574 Gallardo, L. A., Meju, M. A., 2007. Joint two-dimensional cross-gradient imaging of magnetotelluric and
575 seismic traveltimes data for structural and lithological classification. Geophysical Journal International
576 169, 1261–1272, doi:10.1111/j.1365-246X.2007.03366.x.

577 Haber, E., Ascher, U. M., 2001. Fast finite volume simulation of 3D electromagnetic problems with
578 highly discontinuous coefficients. SIAM Journal of Scientific Computing 22, 1943–61.

579 Haber, E., Ascher, U. M., Aruliah, D. A., Oldenburg, D. W., 2000. Fast simulation of 3D electromagnetic
580 problems using potentials. Journal of Computational Physics 63, 150–171.

581 Hermance, J. F., Neumann, G. A., 1991. The Rio Grande rift: New electromagnetic constraints on the
582 Socorro magma body. Physics of the Earth and Planetary Interiors 66, 101–117.

583 Holland, R., 1993. Pitfalls of staircase meshing. IEEE Transactions on Electromagnetic Compatibility
584 35, 434–439.

585 Hursan, G., Zhdanov, M. S., 2002. Contraction integral equation method in three-dimensional electro-
586 magnetic modeling. Radio Science 37, doi:10.1029/2001RS002513.

587 Jackson, J. D., 2002. From Lorenz to Coulomb and other explicit gauge transformations. American
588 Journal of Physics 70, 917–928.

589 Jones, A., Carlson, R., Gruttler, H., 2003. The electrical structure of the Slave craton. Lithos 71, 505–527.

590 LaBrecque, D. L., 1999. Finite difference modeling of 3D EM fields with vector and scalar potentials. In:
591 Oristaglio, M., Spies, B. (Eds.), 3-Dimensional Electromagnetics. Society for Exploration Geophysi-
592 cists, pp. 146–160.

593 Mackie, R. L., Smith, J. T., Madden, T. R., 1994. Three-dimensional modeling using finite difference
594 equations. Radio Science 29, 923–935.

595 Moorkamp, M., Heincke, B., Jegen, M., Roberts, A. W., Hobbs, 2011. A framework for 3-D joint
596 inversion of MT, gravity and seismic refraction data. Geophysical Journal International 184, 477–493,
597 doi:10.1111/j.1365-246X.2010.04856.x.

598 Morisue, T., 1993. A comparison of the Coulomb gauge and Lorentz gauge magnetic vector potential
599 formulations for 3D eddy current calculations. IEEE Transactions on Magnetics 29, 1372–1375.

600 Mukherjee, S., Everett, M. E., 2011. 3D controlled-source electromagnetic edge-based finite element
601 modeling of conductive and permeable heterogeneities. Geophysics 76, F215–F226.

- Newman, G. A., Alumbaugh, D. L., 1995. Frequency-domain modeling of airborne electromagnetic responses using staggered finite differences. *Geophysical Prospecting* 43, 1021–1042.
- Newman, G. A., Alumbaugh, D. L., 2002. Three-dimensional induction logging problems, Part 2: A finite difference solution. *Geophysics* 67, 484–491.
- Oreskes, N., Shrader-Frechette, K., Belitz, K., 1994. [Verification](#), validation and confirmation of models in the Earth sciences. *Science* 263, 641–646.
- Puzyrev, V., Koldan, J., de la Puente, J., Houzeaux, G., Vázquez, M., Cela, J. M., 2013. A parallel finite-element method for three-dimensional controlled-source electromagnetic forward modelling. *Geophysical Journal International* 193, doi: 10.1093/gji/ggt027.
- Ribaudo, J. T., Constable, C. G., Parker, R. L., 2012. Scripted finite element tools for global electromagnetic induction studies. *Geophysical Journal International* 188, 435–446, doi:10.1111/j.1365-246X.2011.05255.x.
- Riedel, M., Bahk, J. J., Scholz, N. A., Ryu, B.-J., Yoo, D.-G., Kim, W., Kim, G. Y., 2012. Mass-transport deposits and gas hydrate occurrences in the Ulleung Basin, East Sea – Part 2: Gas hydrate content and fracture-induced anisotropy. *Marine and Petroleum Geology* 35, 75–90.
- Schenk, O., Gärtner, K., 2004. Solving unsymmetric sparse systems of linear equations with PARDISO. *Future Generation Computer Systems* 20, 475–487, doi:10.1016/j.future.2003.07.011.
- Schenk, O., Gärtner, K., 2006. On fast factorization pivoting methods for sparse symmetric indefinite systems. *Electronic Transactions on Numerical Analysis* 23, 158–179.
- Schwarzbach, C., Boerner, R.-U., Spitzer, K., 2011. Three-dimensional adaptive higher order finite element simulation for geo-electromagnetics-a marine CSEM example. *Geophysical Journal International* 187, 63–74.
- Si, H., 2007. TetGen: a quality tetrahedral mesh generator and 3D Delaunay triangulator. URL-<http://tetgen.berlios.de>.
- Smith, J. T., 1996. Conservative modeling of 3-D electromagnetic fields, Part II: Biconjugate gradient solution and an accelerator. *Geophysics* 61, 1319–1324.
- Stalnaker, J. L., Everett, M. E., Benevides, A., Pierce, C. J., 2006. Mutual induction and the effect of host conductivity on the EM induction response of buried plate targets using 3-D finite-element analysis. *IEEE Transactions on Geoscience and Remote Sensing* 44, 251–259, doi:10.1109/TGRS.2005.860487.
- Streich, C., 2009. 3D finite-difference frequency-domain modeling of controlled-source electromagnetic data: Direct solution and optimization for high accuracy. *Geophysics* 74, F95–F105.
- Sugeng, F., 1998. Modeling the 3D TDEM response using the 3D full-domain finite-element method based on the hexahedral edge-element technique. *Exploration Geophysics* 29, 615–619.
- Tyler, R. H., Vivier, F., Li, S., 2004. Three-dimensional modelling of ocean electrodynamic using gauged potentials. *Geophysical Journal International* 158, 874–887, doi:10.1111/j.1365-246X.2004.02318.x.
- Wait, J. R., 1962. *Electromagnetic Waves in Stratified Media*. Pergamon Press, New York.
- Ward, S. H., Hohmann, G. W., 1987. Electromagnetic theory for geophysical applications. In: Nabighian, M. N. (Ed.), *Electromagnetic Methods in Applied Geophysics. Volume 1, Theory*. Vol. 3 of *Investigations in Geophysics*. Society of Exploration Geophysicists, pp. 131–311.

641 Weiss, C. J., 2001. A matrix-free approach to solving the fully 3D electromagnetic induction problem.
642 SEG Expanded Abstracts 20, 1451–1454.

643 Weiss, C. J., 2010. Triangulated finite difference methods for global-scale electromagnetic induction
644 simulations of whole mantle electrical heterogeneity. *Geochemistry, Geophysics, Geosystems* 11,
645 doi:10.1029/2010GC003283.

646 Weiss, C. J., 2012. Chapter 7. The two- and three-dimensional forward problems. In: Chave, A., Jones,
647 A. (Eds.), *The Magnetotelluric Method: Theory and Practice*. Cambridge University Press, pp. 303–
648 346.

649 Weiss, C. J., Constable, S., Oct 2006. Mapping thin resistors and hydrocarbons with marine EM methods,
650 part II — Modeling and analysis in 3D. *Geophysics*, G321–G332Doi:10.1190/1.2356908.

651 Weiss, C. J., Newman, G. A., 2002. Geomagnetic induction in a fully 3-D anisotropic Earth. *Geophysics*
652 67, 1104–1114.

653 Weiss, C. J., Newman, G. A., 2003. Electromagnetic induction in a generalized 3D anisotropic Earth,
654 Part 2: The LIN preconditioner. *Geophysics* 68, 922–930.

655 Yee, K. S., 1966. Numerical solution of initial boundary problems involving Maxwell’s equations in
656 isotropic media. *IEEE Transactions on Antennas and Propagation* AP-14 (3), 302–307.

657 Zhang, S., Karato, S.-I., 1995. Lattice preferred orientation of olivine aggregates deformed in simple
658 shear. *Nature* 375, 774–777.

659 8. Appendix A. The scattered-field formulation

660 A straightforward extension of Eq (7) and (8) is the case where the potentials are
 661 split into “primary” (\mathbf{A}_0, Φ_0) and “scattered” components (\mathbf{A}_1, Φ_1) such that $\mathbf{A}_0 =$
 662 $\mathbf{A}_0 + \mathbf{A}_1$ and $\Phi_0 = \Phi_0 + \Phi_1$. The split is predicated on the observation that for a given
 663 conductivity model $\sigma = \sigma_0 + \sigma_1$, primary components corresponding to model σ_0 are easy
 664 to compute (typically, by analytic or quasi-analytic formulae) and scattered components
 665 arising from conductivity perturbations $\sigma_1 = \sigma - \sigma_0$ possess some attractive properties
 666 such as compactness or smoothness absent in the total solution. For completeness, the
 667 scattered-field formulation of the Lorenz-gauged potentials follows as,

$$\begin{pmatrix} -\nabla^2 + k^2 & \nabla k^2 - k^2 \nabla \\ \nabla \cdot k^2 - k^2 \nabla \cdot & -\nabla \cdot k^2 \nabla + k^4 \end{pmatrix} \begin{pmatrix} \mathbf{A}_1 \\ \Phi_1 \end{pmatrix} =$$

$$\begin{pmatrix} -k_1^2 & -\nabla k_1^2 + k_1^2 \nabla \\ \nabla \cdot k_1^2 + k_1^2 \nabla \cdot & \nabla \cdot k_1^2 \nabla - k_1^4 - 2k_0^2 k_1^2 \end{pmatrix} \begin{pmatrix} \mathbf{A}_0 \\ \Phi_0 \end{pmatrix}.$$

(A1)

668 Observe that solution to the 3D EM induction problem by secondary potentials from the
 669 total potential formulation only by the assembly of the right-hand-side source vector.

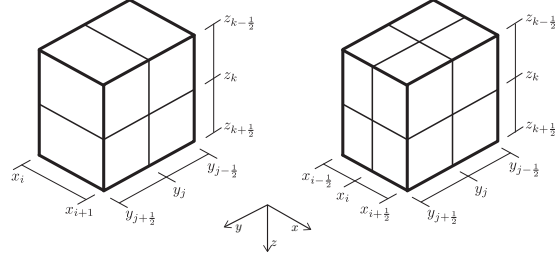


Figure 1: (left) Integration region for finite volume discretization of \hat{x} -component Eq (7) at grid point (x_i, y_j, z_k) . Right, integration region for scalar component of Eq (7) around grid point (x_i, y_j, z_k) .

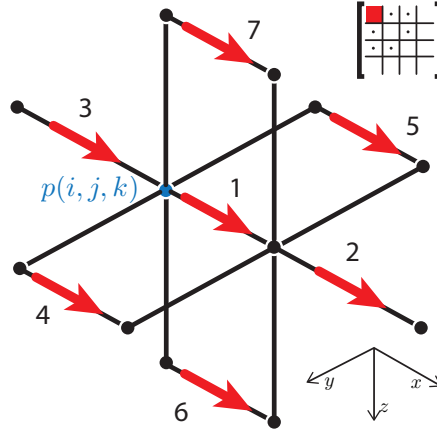


Figure 2: Template for the \hat{x} -directed components of the vector Helmholtz equation for the magnetic vector potential. Block of matrix in Eq (8) to which this \hat{x} template applies (inset).

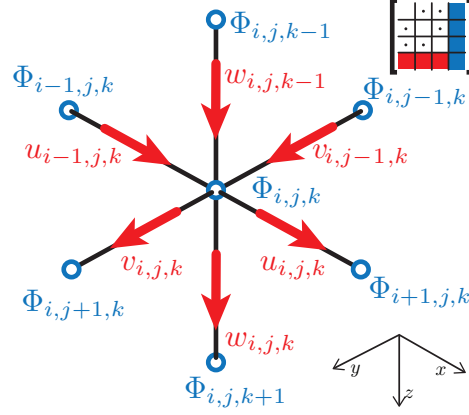


Figure 3: Template for the node-based components of the scalar Poisson equation. Also shown are the corresponding components of the potentials for discretizing the coupling matrices in the last block-column and block-row of full finite volume coefficient matrix in Eq (7). Here, $\mathbf{A} = \hat{x}u + \hat{y}v + \hat{z}w$, where subscripts on these functions and the scalar potential Φ indicate their discrete indexing in the \hat{x} , \hat{y} and \hat{z} directions, respectively. Blocks of the matrix in Eq (7) to which this template and components apply (inset).

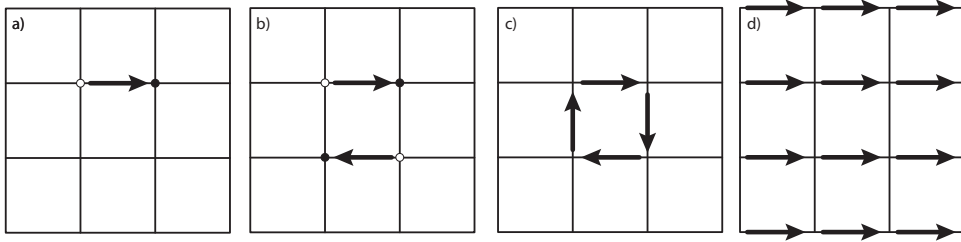


Figure 4: Assemblages of the grid-aligned elementary electric dipole (a) into current couple (b), loop (c), and sheet (d) sources. Galvanic charges present at the dipole terminus (symbols in a and b) arising from the $\nabla \cdot \mathbf{J}_s$ source terms cancel in the case of uniform current density shown here in examples c and d.

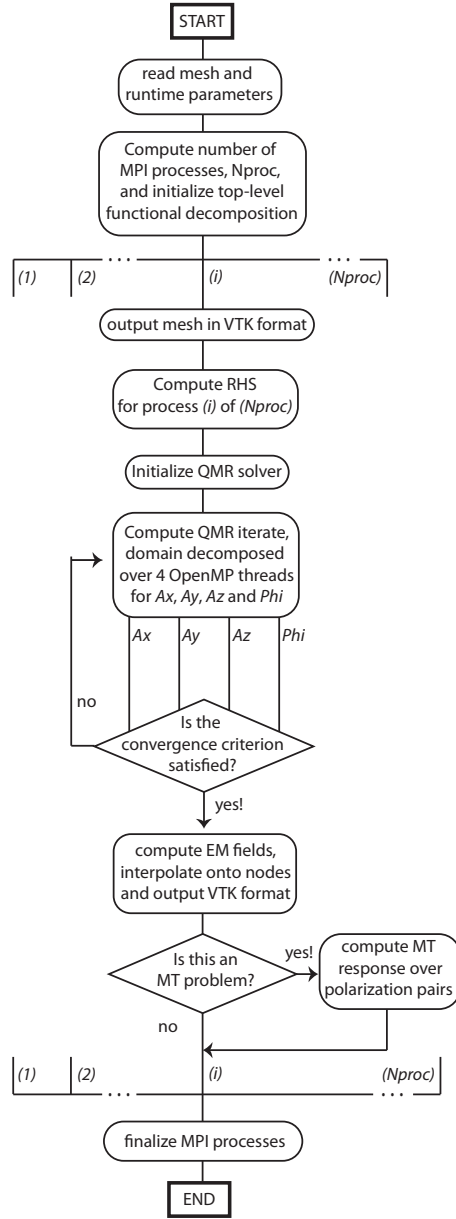


Figure 5: Workflow for functional/domain decomposition over processes and threads for multiple sources and frequencies.

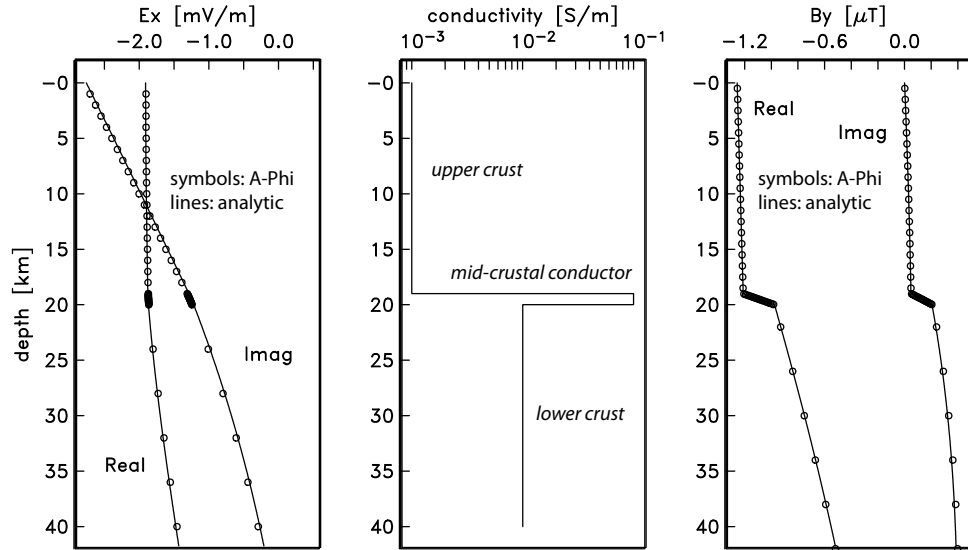


Figure 6: 0.01Hz MT example

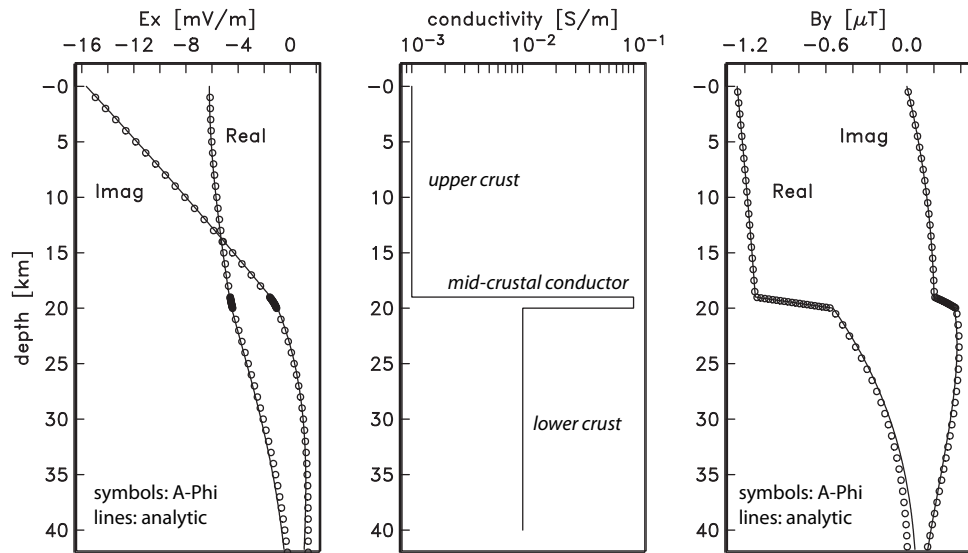


Figure 7: 0.1Hz MT example

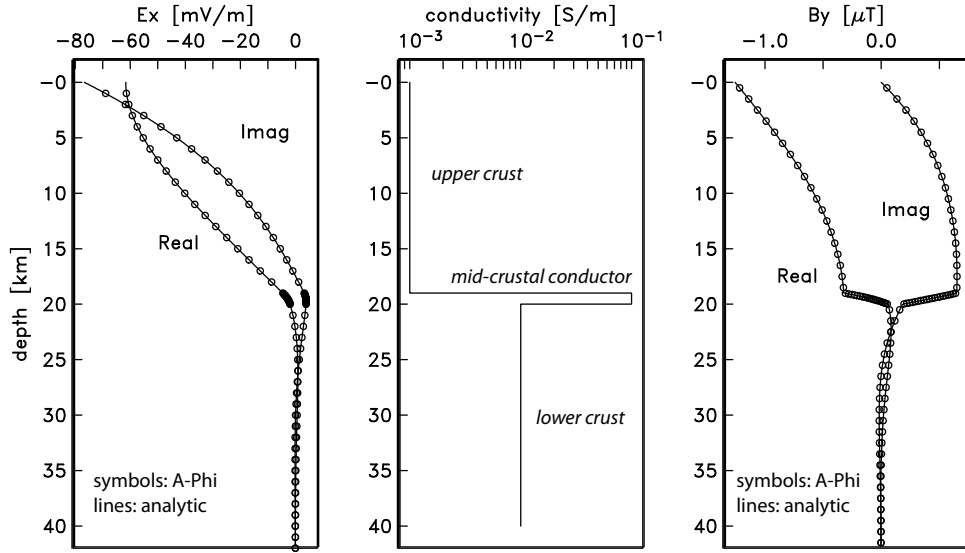


Figure 8: 1Hz MT example

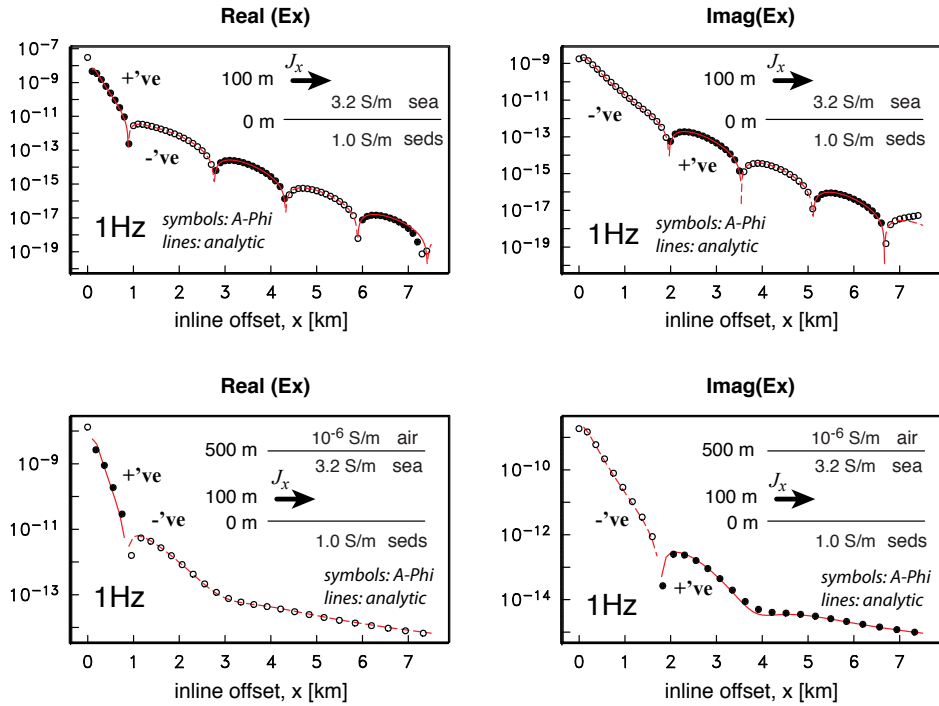


Figure 9: 1Hz CSEM example. Inline horizontal electric field along the seabed for both deep water (top) and shallow water (bottom) models (inset).

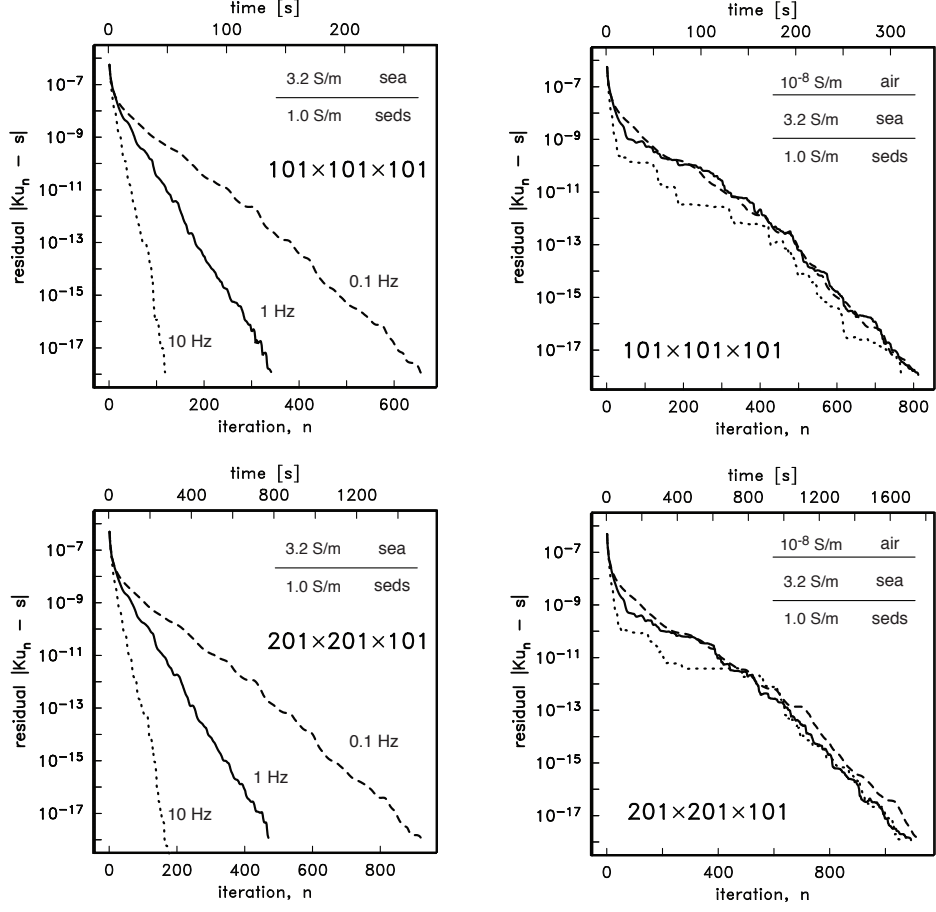


Figure 10: Effect of model frequency, model size and the presence of the air layer on the convergence of the QMR iterative sequence for linear system in Eq (14) corresponding to the CSEM model described in Figure 9. Small $101 \times 101 \times 101$ node models are shown at top, large $201 \times 201 \times 101$ models at bottom.

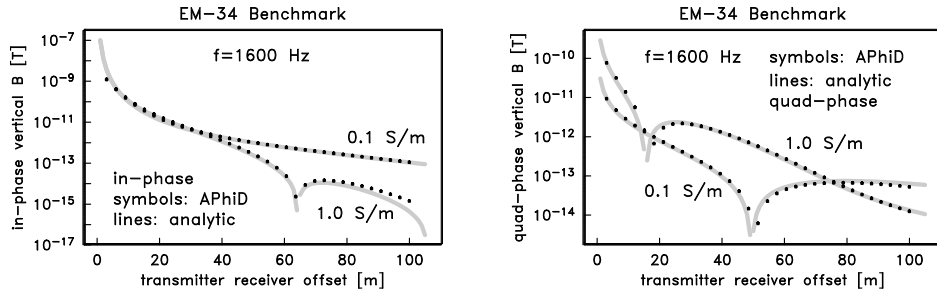


Figure 11: EM34 example for the $f=1.6$ kHz, 20 m offset configuration.

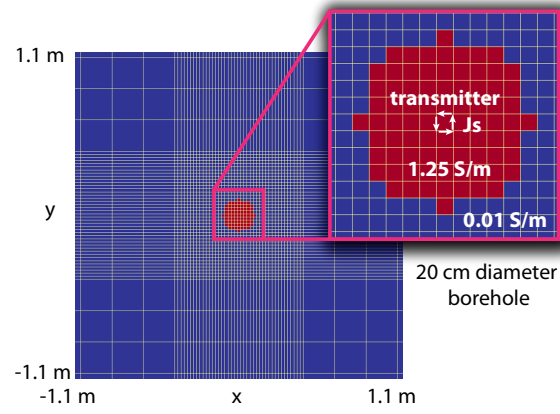


Figure 12: Zoomed in view of $z = 1$ m plane from the conductivity model used for high-frequency borehole simulation, illustrating staircase representation the borehole wall and the square, finite-dimension transmitter antenna, \mathbf{J}_s .

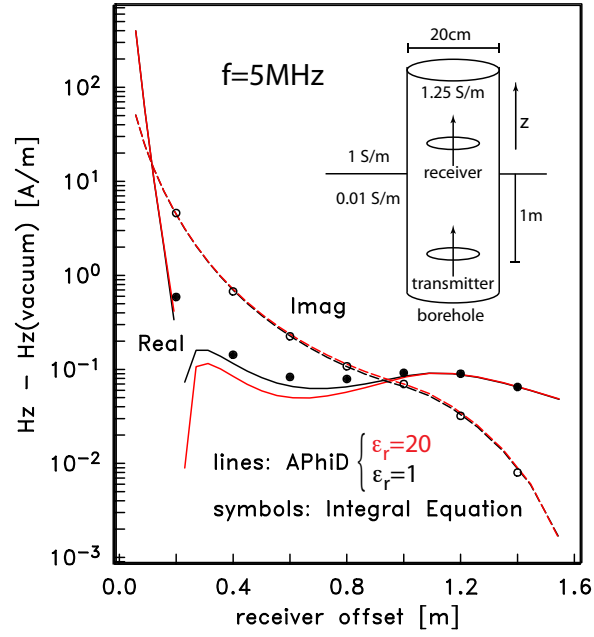


Figure 13: High frequency ($f = 5$ MHz) borehole induction logging example. Simulated here is the response of a single-transmitter, multiple-receiver array configuration situated directly below a bed contact within a conductive borehole drilling fluid (inset). Comparison **between** integral equation (symbols) and numerical solutions (lines) show excellent agreement except at small offsets where the effect of the finite source dipole in the numerical solution is seen in contrast to the infinitesimal dipole used for the integral equation calculation. For reference, field values are also shown for the 0.01 S/m resistive zone with endowed with relative permittivity $\epsilon_r = 20$, illustrating the effect of water saturation on induction log response, even in the presence of conductive (1.25 S/m) drilling fluid. Field values are normalized for unit dipole magnitude.

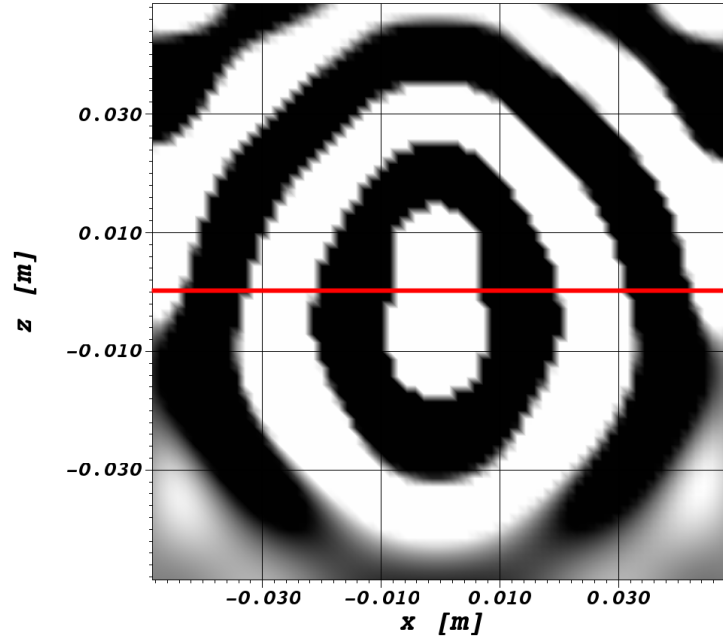


Figure 14: 10 GHz laboratory scale example. Side view of z -directed magnetic induction (imag component) in the $y = 0$ m plane due to a z -directed magnetic dipole source at the origin. Interface separating dielectric contrast is colored red. Grey scale is mapped over the range $\pm 5 \times 10^{-4}$ T.

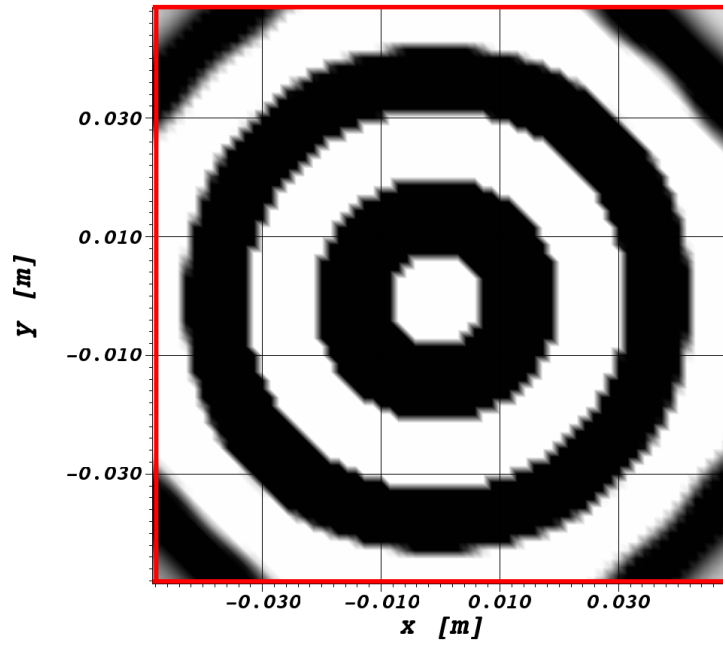


Figure 15: 10 GHz laboratory scale example. Top view of z -directed magnetic induction (imag component) in dielectric interface ($z = 0$ m plane with the perimeter denoted in red). Grey scale is mapped over the range $\pm 5 \times 10^{-4}$ T.

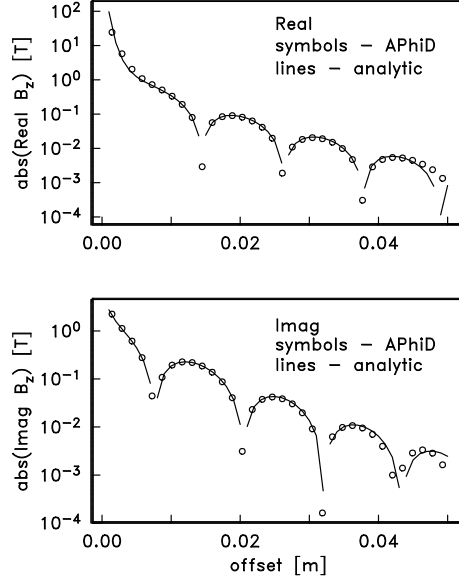


Figure 16: 10GHz laboratory scale example. Comparison between numeric (symbols) and analytic (lines) values of z -directed magnetic induction along dielectric interface as a function of offset from the magnetic dipole source antenna at the origin (see figs 11 and 12).

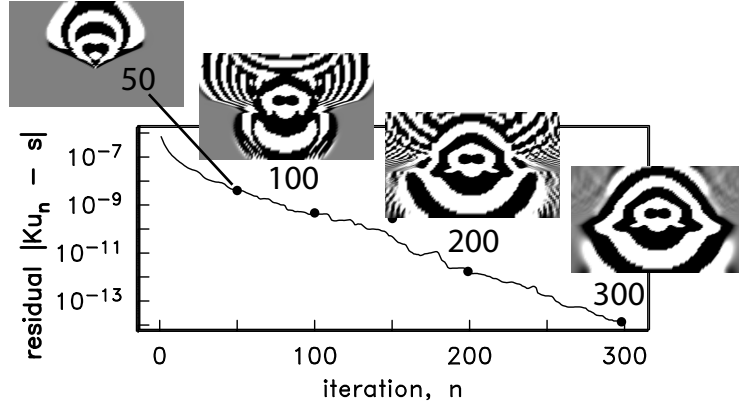


Figure 17: Evolution of the imaginary (Ex) component in the (x, z) at $y = 0$ m as a function of QMR residual for the linear system Eq (14) corresponding to the 1 Hz CSEM problem (no air layer) in Figure (9). Snapshots (inset) show the solution at iterations 50, 100, 200 and 300, grey-scaled on the range $\pm 1 \times 10^{-18}$ V/m.